Temperature-dependent first-order reversal curve measurements on unusually hard magnetic low-temperature phase of MnBi

Shreyas Muralidhar,[1,*] Joachim Gräfe,[1] Yu-Chun Chen,[1] Martin Etter,[2] Giuliano Gregori,[3] Semih Ener,[4] Simon Sawatzki,[4] Kazuhiro Hono,[5] Oliver Gutfleisch,[4] Helmut Kronmüller,[1] Gisela Schütz,[1] and Eberhard J. Goering[1,†]

[1]*Max Planck Institute for Intelligent Systems, Heisenbergstrasse 3, 70569 Stuttgart, Germany*
[2]*Deutsches Elektronen-Synchrotron, Hamburg, Germany*
[3]*Max Planck Institute for Solid State Research, Stuttgart, Germany*
[4]*Institute of Materials Science, Technische Universität Darmstadt, Darmstadt, Germany*
[5]*National Institute for Materials Science, Tsukuba, Japan*

We have performed first-order reversal curve (FORC) measurements to investigate the irreversible magnetization processes in the low-temperature phase of MnBi. Using temperature-dependent FORC analysis, we are able to provide a clear insight into the effects of microstructural parameters such as grain diameter, shape, and surface composition on the coercivity of nucleation hardened permanent magnet MnBi. FORC diagrams of MnBi show a unique broadening and narrowing of the coercive field distribution with increasing temperature. We were able to microscopically identify the reason for this behavior, based on the shift in the single domain critical diameter from nearly 1 to 2 μm, thereby changing the dependence of coercivity with particle size. This is based on a strong increase in the uniaxial anisotropy constant with increasing temperature. Furthermore, the results also give an additional confirmation that the magnetic hardening in low-temperature phase MnBi occurs due to nucleation mechanisms. In our case, we show that temperature-dependent FORC measurements provide a powerful tool for the microscopic understanding of high-performance permanent magnet systems.

I. INTRODUCTION

MnBi is a rare-earth free intermetallic compound with unique magnetic properties. The most important properties of this ferromagnet include a high Kerr response [1,2], a large uniaxial magnetic anisotropy ($K \simeq 10^6$ J/m³) [3–5], and a high coercivity with a large positive temperature coefficient at high temperatures [6], unlike other high-performance permanent magnets. According to the phase diagram [7], there are two important phases of MnBi. The low-temperature phase (LTP), which is ferromagnetic, and the high-temperature phase (HTP), which is paramagnetic. LTP-MnBi is of considerable interest due to its potential role as a substitution for Nd-Fe-B and Sm-Co magnets at high temperatures (425–535 K) [8]. The origin of the positive temperature coefficient is accounted for by the increase of magnetocrystalline anisotropy energy (MAE) due to lattice elongation [9]. At 500 K, LTP-MnBi exhibits a coercive field of about 2.3 T and the maximum energy product $BH_{\max} \sim 10$ MGOe for an anisotropic aligned powder sample. This value is higher than that for many other permanent magnets at 500 K [8].

Synthesis of highly ordered and pure nanocrystalline MnBi requires a well-defined milling and annealing treatment [10–12]. Employing the proper synthesis technique is important to obtain high-performance magnets with large coercive fields (H_c). The theoretical limit for a coercive field is calculated based on the nucleation field (H_N) of an ellipsoidal particle. For LTP-MnBi at room temperature, using the values for K_1 and M_s from Ref. [3], we could estimate the value for the theoretical limit from Eq. (1),

$$H_N = \frac{2K_1}{M_s} \simeq 5.6 \text{ T}, \tag{1}$$

where $M_s = 645$ kA/m is the spontaneous magnetization, and $K_1 = 1.8$ MJ/m³ is the anisotropy constant at room temperature. All experimental values of coercivity reported in the literature are far below this ideal value. This is popularly known as Brown's paradox [13,14], which is influenced by the microstructural parameters such as size, boundary composition, shape, and orientation of the grains. Thus, a better understanding of the magnetic hardening mechanisms in the system is required. According to the micromagnetic analysis performed by Kronmüller *et al.*, the prevailing hardening mechanism in LTP-MnBi is due to nucleation of reversed domains [15]. A recently developed experimental method that involves the measurement of first-order reversal curves (FORCs) has been proven to be effective to study irreversible processes involved in the magnetization reversal [16–19]. It involves a measurement of a series of minor hysteresis loops starting from different reversal field points up to saturation [20]. Further, processing the data using a computational technique first introduced by Roberts *et al.* gives the FORC density map [16]. It is a two-dimensional contour map along the coercive and the interaction field axis. So far no reports have been made on FORC studies of MnBi hard magnets. This may be due to the extensively long measurement durations and the complexity of the analysis of FORC diagrams.

---

*muralidhar.shreyas@gmail.com
†goering@is.mpg.de

According to the theory of micromagnetism, the magnetic hardening mechanisms involved in permanent magnetic materials are closely related to their microstructure [21]. In the case of domain-wall pinning mechanisms, lattice defects play a prominent role in increasing the coercive field [22]. In nucleation hardened materials, the size, shape, and orientation of the grains and the composition of grain and phase boundaries play a key role [23]. To understand the factors contributing to the positive temperature coefficient of the coercive field, we performed a temperature-dependent FORC analysis. Together with a combination of structural and FORC analysis, we present an extension to the existing micromagnetic model, explaining the dependence of nucleation field on the particle diameters at varying temperatures.

II. EXPERIMENTAL METHODS

$Mn_x Bi_{100-x}$ ($x = 45, 55$) ingots were prepared from high-purity manganese and bismuth by arc melting in an argon atmosphere followed by annealing, ball milling, and finally purification by magnetic separation [11]. Powder samples obtained by this method showed a saturation magnetization (M_s) of 72.5 emu/g. High-performance anisotropic magnets were acquired after consolidation by fast hot-compaction (HC) and spark-plasma sintering (SPS) at different temperatures, pressures, and dwell times. For more details on sample preparation, see Ref. [24]. Two samples from each of the consolidation techniques were chosen for basic characterization and FORC analysis. They are as follows:

HC 1: $x = 45$ at. %. Hot compacted at 473 K (200 °C) at 200 MPa pressure for 5 min.

HC 2: $x = 45$ at. %. Hot compacted at 573 K (300 °C) at 200 MPa pressure for 5 min.

SPS 1: $x = 55$ at. %. Spark plasma sintered at 533 K (260 °C) at 120 MPa pressure for 30 s.

SPS 2: $x = 45$ at. %. Spark plasma sintered at 533 K (260 °C) at 120 MPa pressure for 120 s.

All magnetization loops and first-order reversal curves have been measured by a MPMS 3 SQUID-VSM using the oven option for high-temperature measurements. For powder diffraction measurements, we have used two instruments equipped with either a Cu $K\alpha 1$ radiation with $\lambda = 1.540\,49$ Å or Mo $K\alpha 1$ radiation with $\lambda = 0.7093$ Å. Both instruments are capable of operating in a temperature range from -170 to 1000 °C.

III. STRUCTURAL ANALYSIS

A. Microstructure of the bulk magnets

For a microscopic understanding, we will present a detailed structural analysis of the samples. Scanning electron microscope (SEM) images of the polished bulk samples are shown in Fig. 1. In each of these samples, the brightest area corresponds to elemental Bi while the darkest area is Mn. The gray shaded area is the LTP-MnBi. The histogram in the inset shows the particle size distribution, determined by analysis of the SEM images obtained. It shows a log-normal distribution, as expected [26]. The samples SPS 1 and HC 1 have an almost similar particle size distribution with a mean value of around 3 μm. SPS 2 has smaller particles (~ 2 μm),

while the HC 2 sample has the largest average particle size of 4 μm. A clear inverse correlation between the average particle sizes and the coercivity could be observed [Fig. 3(b)], revealing the highest coercivity for the smallest particle sizes and the smallest coercivity for the sample with the largest particles.

Apart from the size of the particles, we can make a rough estimation of the general shape of the majority of grains. In hot compaction samples, the particles are slightly elongated along the easy axis direction, whereas in spark plasma sintered samples we see an irregularity in grain shape irrespective of the direction of the easy axis. The heating rate in the hot compaction process is slow and homogeneous over the sample. This causes grain growth and elongation in the prealignment direction. On the other hand, the spark plasma sintering process is fast and results in local Joule heating, thus restricting the grain growth and subsequent elongation.

The presence of a decoupling layer between the grains further increases the coercivity [27]. In Fig. 1, a clear decoupling layer can be observed. In summary, a number of factors, such as smaller grain diameter, having prolate ellipsoidal shaped grains exhibiting an easy axis along the longer axis of the ellipsoid, and the presence of a decoupling layer between grains, contribute to the increase in coercivity of MnBi.

B. Effect of temperature on lattice dimensions

LTP-MnBi has a hexagonal NiAs-type crystal structure with an easy axis along the c-axis at room temperature [28]. The lattice parameters and its variation with temperature were determined by x-ray diffraction performed on powdered samples in the range 300–550 K. The lattice parameters and phase contents were determined either by Le Bail or Rietveld refinement. Three phase groups were considered to fit the diffraction patterns: LTP-MnBi phase ($P63/mmc$, $a = 4.291$ Å, $c = 6.123$ Å), α-Mn ($I\bar{4}3m$, $a = 8.921$ Å), and Bi ($R\bar{3}m$, $a = 4.547$ Å, $c = 11.872$ Å). As expected, due to thermal expansion of solids, the volume of the unit cell increases with temperature. This is shown in the inset of Fig. 2. Each individual sample has a different initial unit-cell volume, but the slopes of the curves do not vary much. Figure 2 represents the variation of the c/a ratio with an increase in temperature. An interesting behavior observed from this is the vertical elongation of the hexagonal lattice with temperature. The linear increase of the c/a ratio not only reflects the increase in volume, but it also denotes an increase in anisotropy and related anisotropy constant (K_1) [9]. The c/a values are in good agreement with other reports [29].

IV. MAGNETIC CHARACTERIZATION

The magnetocrystalline anisotropy of MnBi increases with increasing temperature [9]. A direct consequence of that is the temperature-dependent coercivity, shown in Fig. 3(a). It is determined from the major hysteresis loops at various temperatures. In general, MnBi exhibits a steep increase in the coercivity from room temperature up to 550 K. From 300 K down to 100 K there is a gradual but a very small decrease in the coercive field. The slopes of the curve at high temperatures for all the samples are nearly the same. At all temperatures, SPS 2
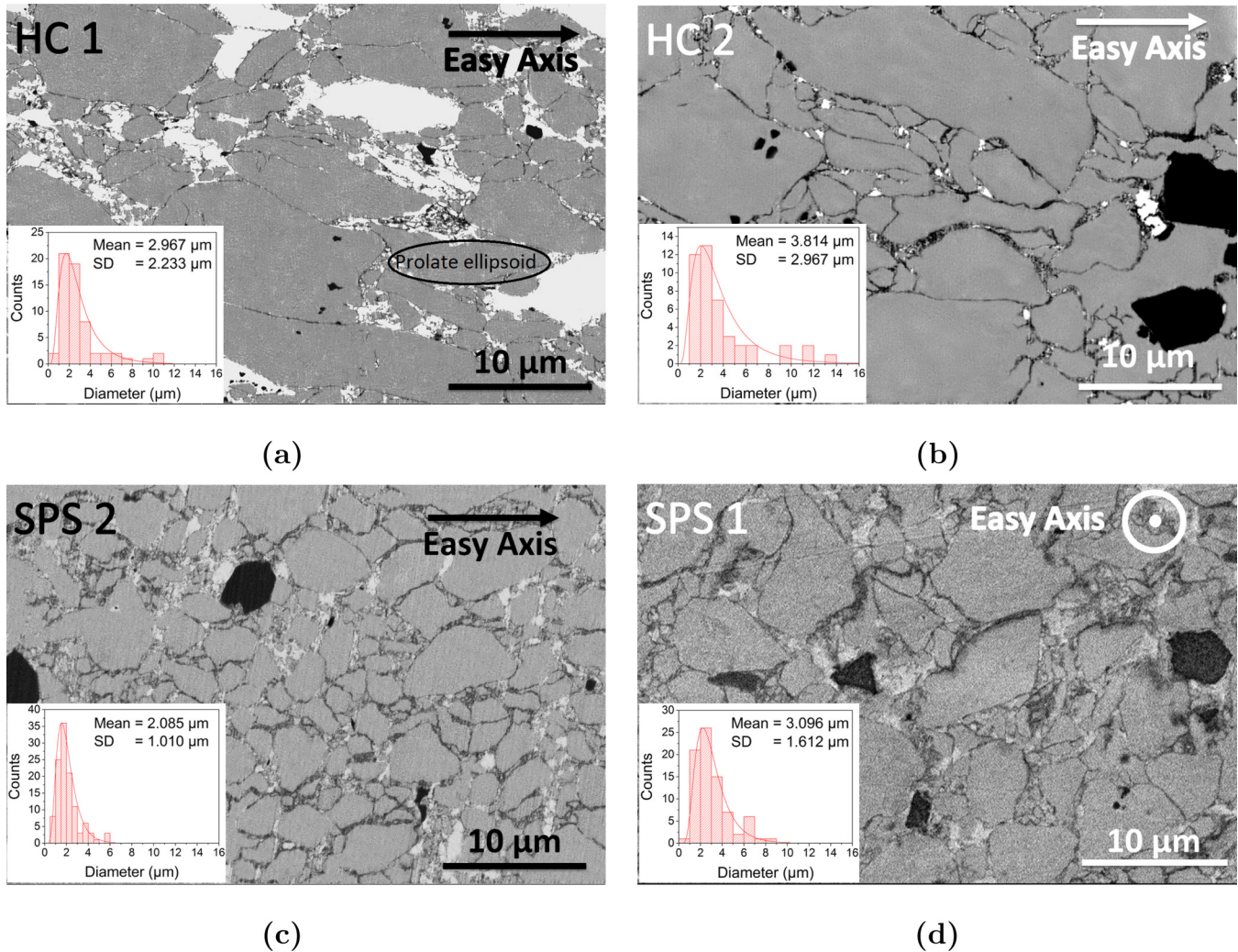
FIG. 1. SEM images of the samples (a) HC 1, (b) HC 2, (c) SPS 2, and (d) SPS 1. The alignment direction (easy axis) is indicated on the top right corner of all images. The inset shows the particle size distribution of each of the samples. Hot compacted samples in particular have elongated particles in the direction of alignment (prolate ellipsoid) [25]. Spark-plasma sintered samples, on the other hand, have irregularly shaped particles.
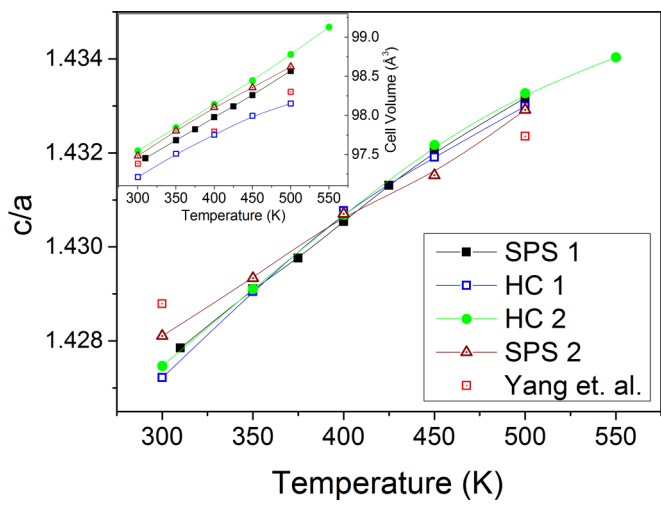

FIG. 2. Variation of lattice parameters for hexagonal LTP-MnBi with temperature for the four samples. The inset shows the unit-cell volume with temperature.

has the largest coercivity ($H_c = 6500$ Oe at 300 K). HC 2, on the other hand, has the smallest coercivity ($H_c = 750$ Oe at 300 K). The temperature-dependent coercive field for the samples HC 1 and SPS 1 is identical, as seen in the Fig. 3(a). The HC samples have higher saturation magnetization and a higher remanence ratio (M_r/M_s) compared to the SPS samples [see Fig. 3(b)]. This indicates that the alignment of grains is better in the HC samples.

V. FORC ANALYSIS

A. First-order reversal curve method

The FORC method is a way of accessing the magnetization behavior of the material. It involves the measurement of a multitude of minor hysteresis loops commonly referred to as first-order reversal curves. The mathematical model [20] was first proposed by Mayergoyz in 1986 to find experimental access to the Preisach distribution [30] for a hysteretic system. He also derived the necessary and sufficient conditions for the direct agreement between FORC and Preisach distributions.
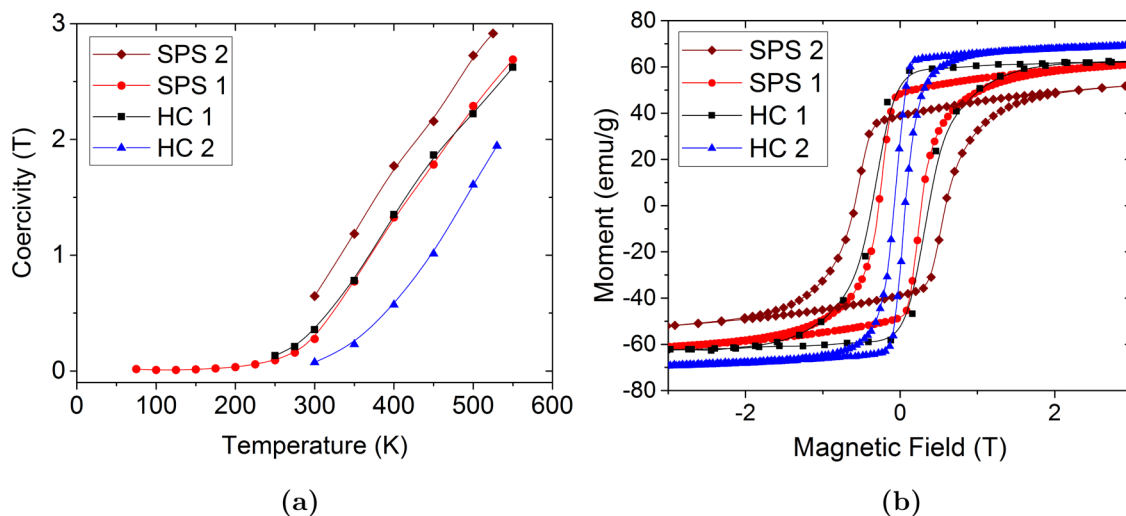
FIG. 3. (a) Coercive field vs temperature for different samples. (b) Hysteresis loops for all the samples at 300 K. See the text for a detailed description.

Later, Pike, Roberts, and collaborators conducted the first experimental procedure on geological samples [16]. Additional studies using FORC were based on nanostructured array systems [17,18,31–34], nanocrystalline [35,36], and hard magnetic materials [19]. The FORC measurement starts in magnetic saturation. Subsequently, the field is reduced to a particular reversal field (H_r), and the minor loop is then recorded by increasing the applied field (H) gradually back to the saturation field. The FORC density is a mixed second-order derivative of the magnetization as a function of reversal field (H_r) and applied field (H),

$$\rho(H, H_r) = -\frac{1}{2} \frac{\partial^2 M(H, H_r)}{\partial H \partial H_r}. \tag{2}$$

Numerically, the FORC density is calculated by fitting a two-dimensional (2D) polynomial [16],

$$M(H, H_r) = a_0 + a_1 H + a_2 H_r + a_3 H^2 + a_4 H_r^2 - 2a_5 H H_r, \tag{3}$$

onto a local square grid of data and determining the parameter a_5, which is the FORC density,

$$\rho(H, H_r) \equiv a_5 = -\frac{1}{2} \frac{\partial^2 M(H, H_r)}{\partial H \partial H_r}. \tag{4}$$

A FORC diagram is a contour plot of the FORC density along the coercive (H_c) and interaction (H_u) field axis [16] given by

$$H_u = \frac{H + H_r}{2}, \tag{5}$$

$$H_c = \frac{H - H_r}{2}. \tag{6}$$

The size of the local square grid of data used to fit the polynomial is given by the smoothing factor (SF). The resolution of the FORC diagram is then given by

$$R = 2 \times SF \times \Delta H, \tag{7}$$

where ΔH is the field step width [37]. Note, the calculation of FORC density is based on an extended FORC formalism [38]

where the magnetization $M(H, H_r)$ for $H < H_r$ is assumed to be $M(H, H_r = H)$.

The calculation of FORC density and construction of FORC diagrams were done by a code developed in MATLAB [39] to efficiently treat data from Quantum Design MPMS 3 SQUID-VSM. The technique has been proven effective due to the large amount of information provided. Even though the measurement and computation of a FORC diagram is time-consuming, the method yields a clear picture of the switching fields and the local interaction fields that are otherwise not extractable from simple hysteresis loop. In the current paper, we present the temperature-dependent FORC diagrams of MnBi samples.

B. FORC diagrams

The FORC diagrams were obtained at different temperatures ranging from 250 to 535 K. To avoid structural changes due to eutectic reaction [12] in the material, we restrict our measurements up to 535 K, despite the fact that thermal stability of LTP-MnBi up to 650 K has been reported [11]. Hence we resort to temperatures lower than 535 K during FORC analysis except for one sample (HC 1).

It is necessary to have a low noise measurement. Since the FORC density is a double partial derivative of the magnetization, any noise in the raw data will be strongly pronounced. Each FORC measurement routine included nearly 150 individual minor loops, measured in a range of −5 to +5 T, with a field sweep rate of 0.01 T/s. This rate was chosen as a tradeoff between achieving the optimum response time from a hard magnetic material such as MnBi and avoiding excessive measurement time. Optimizing the smoothing factor and the interpolation steps gives a balance between good resolution and low noise. The FORC diagrams obtained in this way are shown in Fig. 4.

1. HC 1

Figure 4(a) shows the FORC diagrams for the sample HC 1 at 300, 400, 500, and 550 K with a resolution of 0.05, 0.05,
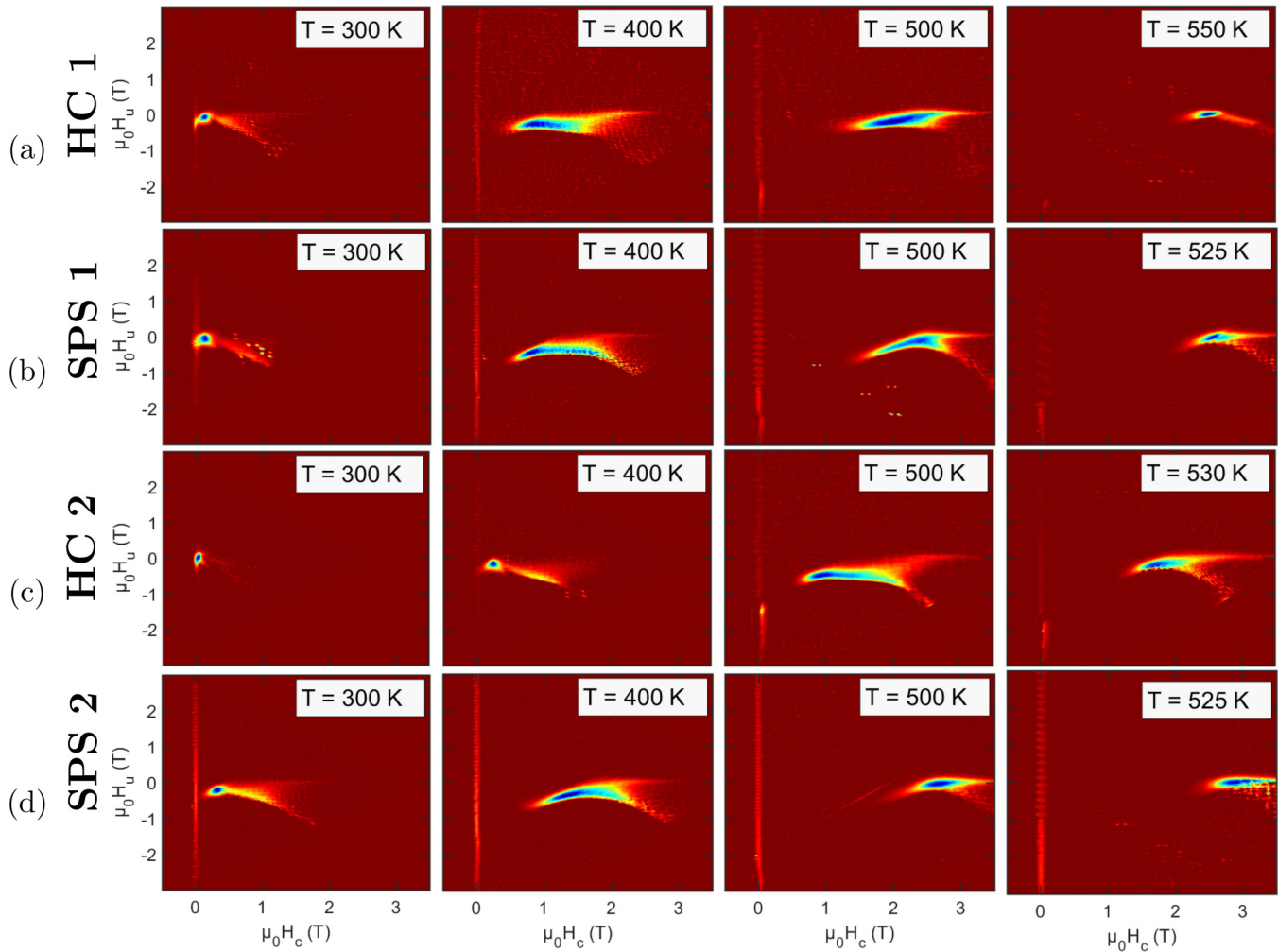
FIG. 4. FORC diagrams of the LTP-MnBi hard magnet with uniaxial anisotropy. (a) HC 1, hot compacted at 473 K. Mean diameter of the particles is 2.97 μm (b) SPS 1, spark plasma sintered at 533 K. Mean diameter is 3.10 μm (c) HC 2, hot compacted at 573 K. Mean diameter is 3.81 μm (d) SPS 2, spark plasma sintered at 533 K with an atomic ratio of Mn:Bi as 45:55. Mean diameter of the particles is 2.09 μm. The temperature is given at the top right corner of each of the FORC diagrams.

0.08, and 0.1 T, respectively. At 300 K, the contribution to the irreversible magnetization reversal processes is represented as a single peak centered at $H_c = 0.15$ T, and a butterfly wing feature extends along the coercivity axis. The coercive field of the sample as determined from the major hysteresis loop at 300 K is $H_c = 0.36$ T (see Fig. 3). At 400 K this increases to 1.35 T. The FORC density map shows a shift and an expansion of the peak along the coercivity axis with increasing temperature. The width of the peak is about 1.2 T, and it is centered at $H_c = 0.85$ T. There is a very small shift of the peak along the interaction field axis. For the FORC diagram at 500 K, the peak is centered around 2.2 T and the width of the peak is nearly the same. In this case, we have performed a measurement at 550 K, which represents a FORC peak that is very narrow and centered at $H_c = 2.5$ T.

2. SPS 1

The FORC density maps for the sample SPS 1 are given in Fig. 4(b). The resolutions of these FORC diagrams at 300, 400, 500, and 525 K are 0.08, 0.05, 0.07, and 0.13 T, respectively. At first glance, the FORC diagrams look very similar to that

for HC 1. Indeed, they are very similar in terms of the FORC density peak position and width. At 300 K, a Gaussian peaklike feature centered at $H_c = 0.12$ T with a butterfly wing structure is observed. At 400 K, it shows a broad peak with a width of about 1.3 T. At higher temperature, it shows a slightly narrower peak ($\sim$1 T) already at 500 K. The FORC peak at 525 K is just 0.5 T wide located at $H_c = 2.54$ T.

3. HC 2

Sample HC 2 has the smallest coercive field. Figure 4(c) displays the FORC diagrams at 300, 400, 500, and 530 K with a resolution of 0.04, 0.05, 0.08, and 0.11 T, respectively. The coercivity from the major hysteresis loop at 300 K for this sample is 0.07 T. The FORC density peak is a sharp peak located at this point on the H_c axis. At 400 K, the FORC density map shows two irreversible features similar to the FORC diagram for HC 1 [Fig. 4(a)] and SPS 1 [Fig. 4(b)], both at 300 K. In accordance with the previous trend, the density peak at 400 K undergoes a shift and an expansion along the coercive field axis to form the peaks at 500 K. This is similar to the peaks in sample SPS 1 and HC 1 at 400 K;
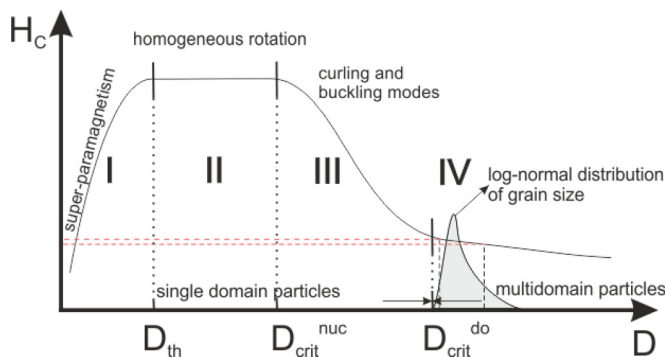
FIG. 5. Schematic representation of a coercive field dependent on particle diameter adopted from Ref. [40].

Figs. 4(a) and 4(b). At an elevated temperature (530 K), the FORC diagram shows a narrower peak.

4. SPS 2

Unlike HC 2, SPS 2 has smaller particles and correspondingly greater coercivity. Figure 4(d) shows the FORC diagrams for sample SPS 2 at 300, 400, 500, and 525 K. The resolutions of these FORC maps are 0.05, 0.05, 0.13, and 0.15 T, respectively. At 300 K, the peak is centered at $H_c = 0.33$ T and there is a prominent butterfly wing extension at higher switching fields. The coercivity as measured from the major hysteresis loop is 0.65 T. The FORC density peak at 400 K is a broad peak ($\sim$1.2 T) centered at $H_c = 1.37$ T. At 500 K it is clearly seen that the density peak is narrow again and centered at $H_c = 2.7$ T, which is the coercivity of the sample at 500 K. Compared to the FORC diagrams for sample HC 1 and SPS 1, SPS 2 shows an earlier broadening with increasing temperature.

Summarizing the temperature-dependent FORC diagrams for all the samples, we observed a narrow-broad-narrow distribution of the FORC density peak along the H_c axis accompanied by a translation in the direction of increasing coercive field. Apart from that, there was also a small shift along the negative interaction field. Sample SPS 2 with smaller particles has an earlier onset of broadening of the FORC density peak with increasing temperature, followed by HC 1 and SPS 1, and finally the HC 2 sample having larger particles. The presence of the reversible ridge at $H_c = 0$ T is due the extended FORC formalism [38].

VI. DISCUSSION

A. Theory of micromagnetism

The nucleation field of a magnetic material is mainly dependent on its grain size [40], as shown in Fig. 5. Particles of the order of several microns, in region IV, are in a multidomain state. The magnetization reversal occurs due to nucleation of domain walls through the material and at low coercive fields. The performance of the magnetic material in this region can be improved by domain-wall pinning forces. In the single-domain state, the nucleation of reversed domains occurs in three different modes. Typical permanent magnets undergo (a) homogeneous rotations for particles that are in the size range of about tens of a nanometer, (b) curling, and (c) buckling modes

for particle sizes in a range up to the micron range [40]. The coercive field is independent of the particle size for particles in the homogeneous rotation mode. In contrast, for particles in the curling and buckling modes, the coercive field shows an inverse square-law dependence with respect to grain size [40] (Fig. 5). As an example, we show in Fig. 5 a sample-size distribution, located in the domain-wall rotation regime, that results in a quite narrow coercive field distribution, because of the small slope of the $H_C(D)$ diagram in that range of the size distribution. This corresponds with the room-temperature case of our MnBi samples, as will be shown further in Sec. VI B. Therefore, for a given log-normal distribution of the particle size, a small spread in the coercivities is seen. In this section, we will have a look into the temperature-dependent variation in the nucleation model. The factors that are affected by heating are the critical diameters for the formation of domains ($D_{\text{crit}}^{\text{do}}$) and for the nucleation processes ($D_{\text{crit}}^{\text{nuc}}$).

B. Critical diameters

1. Critical diameter for nucleation processes

The critical crossover diameter, $D_{\text{crit}}^{\text{nuc}}$, between homogeneous rotation and curling processes is obtained by equating the nucleation field expression for both processes [40]. This is given by

$$D_{\text{crit}}^{\text{nuc}} = 3.68 \sqrt{\frac{2A}{N_\perp \mu_0 M_s^2}}, \qquad (8)$$

where μ_0 is the magnetic permeability in vacuum, $N_\perp$ is the demagnetization factor for magnetization perpendicular to the long axis [25], and A is the exchange stiffness constant.

The temperature dependence of the exchange stiffness constant is determined by $A(T) \sim M_s^2(T)$ [40]. Thus, from Eq. (8) it can be seen that the critical diameter for the nucleation processes does not vary with temperature. However, $D_{\text{crit}}^{\text{nuc}}$ also depends on the demagnetization factors of the grains and therefore on details of the microstructure. For example, in sample HC 1 with $N_\perp = 0.435$, $A = 8 \times 10^{-12}$ J/m, and $M_s = 645$ kA/m [3], $D_{\text{crit}}^{\text{nuc}}$ was found to be 30.9 nm. $N_\perp$ was calculated from the ellipticity measured from the SEM image. The value of $N_\perp$ for prolate ellipsoidal particles [25] can vary in the range $0.33 < N_\perp < 0.5$. Therefore, the values of the critical nucleation diameter can only vary over a small range.

2. Critical diameter for single domains

The expression for $D_{\text{crit}}^{\text{do}}$ is obtained by comparing the magnetic energy of a single-domain state and an equivalent two-domain state. A single-domain state is characterized by the stray field of a homogeneously magnetized ellipsoidal particle. A two-domain state is characterized by an additional domain-wall energy, and the stray field energy is reduced by a factor α [40]. The expression for the critical size for a single domain is then given by

$$D_{\text{crit}}^{\text{do}} = \frac{3\gamma_B}{N_\parallel (1-\alpha) \mu_0 M_s^2}, \qquad (9)$$

where γ_B is the domain-wall energy, $N_\parallel$ is the demagnetization factor for magnetization parallel to the long axis, and α is the reduction factor.

TABLE I. Critical single-domain diameters for LTP-MnBi as a function of temperature.

Temperature (K)	K_1[a] (MJ/m³)	M_s[a] (kA/m)	D_{crit}^{do} (μm)
200	0.91	695	0.92
250	1.40	670	1.18
300	1.80	645	1.39
350	2.10	615	1.58
400	2.25	585	1.71
450	2.30	550	1.84
500	2.18	510	1.94
550	2.00	460	2.06
600	1.76	410	2.16

[a]The values for K_1 and M_s are obtained from Guo *et al.* [3].

For uniaxial crystals like MnBi, the expression for domain-wall energy is given by $\gamma_B = 4\sqrt{AK_1}$. For a permanent magnet, typical values for the exchange stiffness constant, A, are in the order of 10^{-12} J/m. The anisotropy constant, K_1, is of the order 10^5–10^6 J/m³. Again, $A(T) \sim M_s^2(T)$. The change in the anisotropy constant [$K_1(T)$] shifts the critical diameter for a single domain by a considerable factor. For a prolate ellipsoidal particle (see Fig. 1), the demagnetization factor $N_\parallel < \frac{1}{3}$ [25]. Furthermore, Eq. (9) shows that for elongated MnBi particles with $N_\parallel \ll 1$, the critical diameters are very large, of the order of several microns.

3. D_{crit}^{do} versus temperature for LTP-MnBi

For LTP-MnBi, the variation of the threshold point (D_{crit}^{do}) with temperature is determined from Eq. (9). The calculations are done for only one sample, HC 1, as an example. Table I shows the values of the critical diameters for domain formation at various temperatures as calculated by using Eq. (9). The values used as parameters in the equation are as follows:

(i) $N_\parallel = 0.13$: this is an average value calculated by measuring approximately the axis lengths of the particles from the SEM image [Fig. 1(a)].

(ii) $\alpha = 0.5$: stray field reduction factor for spherical particles [40].

(iii) $A = 8 \times 10^{-12}$: exchange stiffness constant of MnBi at room temperature [3]. The values of A at other temperatures are calculated by the scaling factor obtained from the temperature-dependent values of M_s^2.

C. Temperature-dependent model

Now, with the reasonable assumption that the expansion of the particles with temperature is negligible, we can keep the distribution of particle diameters constant. Using the values for critical diameters mentioned in Table I, we come to a conclusion that the coercivity of the sample depends mainly on the type of the nucleation processes and the shift of the critical single domain diameter with temperature, as illustrated schematically in Fig. 6.

We consider three different temperatures:

T1: At temperature T1, the grain size distribution lies in the region above the critical diameter for a single domain $D1_{crit}^{do}$. The width of the particle size distribution is represented by the
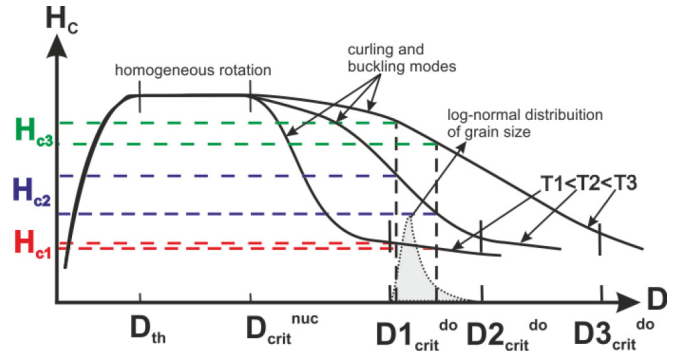

FIG. 6. Schematic representation of the variation of the nucleation field dependence on the particle diameter with increasing temperature for LTP-MnBi.

dotted black lines. Since the slope of the curve in this range is close to zero, a narrow distribution in the coercive field H_{c1} represented by red dotted lines is observed. In the FORC diagrams at low temperature, we can see the narrow density peaks.

T2: As we move to a higher temperature T2, the grain distribution falls in the single-domain range ($D < D2_{crit}^{do}$), where $D2_{crit}^{do}$ is the increased critical diameter. The inhomogeneous nucleation process dominates in this range. The slope of the curve is maximum. Hence the smallest particles correspond to higher coercivity and the largest particles to lower, thus giving a broad distribution of coercivity (H_{c2}) represented by blue dotted lines for the same distribution of particles. The broadening and shift could be observed in the FORC diagrams at intermediate temperatures ∼400 K.

T3: Finally at $T =$ T3, the narrow coercive field distribution (green dotted line) for the same particle size distribution corresponds to the reduced slope of the curve due to increasing critical diameter $D3_{crit}^{do}$. At 530 K, the FORC peaks are nearly as narrow as those at 250 K. See the Supplemental Material [41].

The variation of the FORC distribution with temperature (Fig. 4) for different samples can be explained by the above model based on their grain geometry. Let us consider the sample HC 1 and SPS 1. At low temperatures, the particles lie in the multidomain state. The coercivity of the material is dependent on the nucleation of domain walls through the sample. At room temperature, the initial spread in the coercivity is due to the smallest particles, which fall in the region of single-domain particles. Since the particles are decoupled, the interaction is minimal and based on stray field distributions. At 400 K, the FORC diagram, featuring a wide distribution, corresponds to the nucleation processes curling and buckling. The coercivities of individual particles are size-dependent in this region. From Fig. 6 we can gather that at higher temperatures, the width of the coercivity distribution gets narrower. This can be seen clearly in the FORC diagrams for all the samples at temperatures above 500 K. If the particles are small enough, in the range where the homogeneous rotation process dominates, then the FORC density map would exhibit a single Gaussian peak at the highest coercivity.

The samples HC 2 and SPS 2, on the other hand, show a delayed and earlier onset of the broadening pattern, respectively,

of the temperature-dependent FORC density peaks. While HC 2 at room temperature shows a single narrow peak, SPS 2 has a quite broad distribution. Similarly, at 400 and 500 K, the FORC patterns are slightly shifted to the lower and higher coercivity range compared to the FORC diagrams of HC 1 and SPS 1. A direct correlation between the particle size distribution and the coercive field is observed. The mean size of the particles is smaller in the case of SPS 2 and larger in the case of HC 2 (see Fig. 1).

Even though the mean diameter for the HC 1 sample is slightly larger than that for the SPS 1 sample, a corresponding shift in the pattern of the temperature-dependent FORC density along the coercivity axis is not observed in Fig. 4. Apart from the particle diameters, the demagnetization factors along the perpendicular ($N_\perp$) and parallel ($N_\parallel$) axis play a prominent role in determining the absolute value of the critical diameters. From the SEM images of the lateral section, it was observed that the particles in sample SPS 1 were platelet-like. The demagnetization factor along the easy axis is then given by $N_\perp$ for an oblate spheroid particle [25]. Since the values are always large, the critical domain size is smaller when compared to that for sample HC 1. Hence the two samples show a similar trend in the dependence of FORC diagrams on temperature. Since a completely quantitative analysis requires an accurate measurement of all the parameters involved, the results obtained here are only semiquantitatively explained.

VII. CONCLUSION

Since the discovery of ferromagnetic behavior of MnBi, attempts have been made to understand the high-temperature properties of the system. Studies have been made and new synthesis techniques have been employed based on macroscopic understanding of the hysteresis behavior. Using the FORC method in combination with a structural analysis of the material, we have been able to find a model for the microscopic reversal mechanism (the transition between different nucleation regimes) with temperature. The influence of particle size, shape, and composition is carefully studied. The temperature-dependent FORC diagrams (Fig. 4) show a unique narrow-broad-narrow distribution along the coercive field axis. At room temperature, all the particles lie in the multidomain range. Upon heating, there is an increase in

the critical single-domain diameter, and the particles are at intermediate temperature in the single-domain state, while the coercivity depends on the particle size according to a $1/R^2$ law [40]. Hence, a broad size distribution of the particles gives a broad distribution of coercivities. Finally, at 500 K and above, the particles are close to the threshold for homogeneous processes, and this gives a narrower distribution of coercive fields. The observed trend in the FORC diagrams is also proof that the nucleation mechanisms prevail in the magnetization reversal of MnBi permanent magnets. Comparing the microstructures and FORC maps of different samples, we conclude that well decoupled prolate LTP-MnBi particles with an average particle diameter less than 1 μm are most suitable as a high-performance magnet. Tailoring the synthesis technique effectively to produce them will be the focus of further research.

In general, we demonstrate here that FORC investigations provide extensive details in comparison to conventional major loop investigations. This is because the latter provides details of the change in coercive fields, which is of course related to a simple shift of the internal coercive field distribution. FORC can provide additional knowledge on the related change in the width of the distribution. As we demonstrated here, this width of distribution is directly linked to the hardening mechanisms, which are most important in hard magnet research and are quite often under strong debate. We also want to encourage other researchers to use FORC for permanent magnet investigations, such as a temperature-dependent study of the coercive field distribution. For example, as we show here, if a broadening along the coercive field axis is observed, one can directly estimate that the sample is at the transition between domain-wall pinning and single-domain behavior. Thus we demonstrate that FORC is a "new" and valuable probe for hard magnet investigation.

ACKNOWLEDGMENTS

---

[1] K. Egashira and T. Yamada, J. Appl. Phys. **45**, 3643 (1974).

[2] D. Chen and Y. Gondo, J. Appl. Phys. **35**, 1024 (1964).

[3] X. Guo, X. Chen, Z. Altounian, and J. O. Ström-Olsen, Phys. Rev. B **46**, 14578 (1992).

[4] P. A. Albert and W. J. Carr, J. Appl. Phys. **32**, S201 (1961).

[5] W. E. Stutius, T. Chen, and T. R. Sandin, AIP Conf. Proc. **18**, 1222 (1974).

[6] C. Guillaud, J. Phys. Radium **12**, 492 (1951).

[7] T. Chen, J. Appl. Phys. **45**, 2358 (1974).

[8] J. Park, Y.-K. Hong, J. Lee, W. Lee, S.-G. Kim, and C.-J. Choi, Metals **4**, 455 (2014).

[9] V. P. Antropov, V. N. Antonov, L. V. Bekenov, A. Kutepov, and G. Kotliar, Phys. Rev. B **90**, 054404 (2014).

[10] N. V. R. Rao, A. M. Gabay, and G. C. Hadjipanayis, J. Phys. D **46**, 062001 (2013).

[11] Y.-C. Chen, G. Gregori, A. Leineweber, F. Qu, C.-C. Chen, T. Tietze, H. Kronmüller, G. Schütz, and E. Goering, Scr. Mater. **107**, 131 (2015).

[12] J. Cui *et al.*, J. Phys.: Condens. Matter **26**, 064212 (2014).

[13] W. F. Brown, Phys. Rev. **105**, 1479 (1957).

[14] W. F. Brown, Rev. Mod. Phys. **17**, 15 (1945).

[15] H. Kronmüller, J. B. Yang, and D. Goll, J. Phys.: Condens. Matter **26**, 064210 (2014).

[16] A. P. Roberts, C. R. Pike, and K. L. Verosub, J. Geophys. Res.: Solid Earth **105**, 28461 (2000).

[17] C. R. Pike, C. A. Ross, R. T. Scalettar, and G. Zimanyi, Phys. Rev. B **71**, 134407 (2005).

[18] C.-I. Dobrot and A. Stancu, J. Appl. Phys. **113**, 043928 (2013).

[19] H. Chiriac, N. Lupu, L. Stoleriu, P. Postolache, and A. Stancu, J. Magn. Magn. Mater. **316**, 177 (2007).

[20] I. D. Mayergoyz, Phys. Rev. Lett. **56**, 1518 (1986).

[21] H. Kronmüller, R. Fischer, M. Seeger, and A. Zern, J. Phys. D **29**, 2274 (1996).

[22] H. Kronmüller and D. Goll, Scr. Mater. **47**, 545 (2002).

[23] H. Kronmüller, K.-D. Durst, and M. Sagawa, J. Magn. Magn. Mater. **74**, 291 (1988).

[24] Y.-C. Chen, S. Sawatzki, S. Ener, H. Sepehri-Amin, A. Leineweber, G. Gregori, F. Qu, S. Muralidhar, T. Ohkubo, K. Hono, O. Gutfleisch, H. Kronmüller, G. Schütz, and E. Goering, AIP Advances **6**, 125301 (2016).

[25] B. D. Cullity and C. D. Graham, *Introduction to Magnetic Materials* (Wiley, Hoboken, New Jersey, 2011).

[26] A. N. Kolmogoroff, Dokl. Akad. Nauk SSSR **31**, 99 (1941).

[27] A. Zern, M. Seeger, J. Bauer, and H. Kronmüller, J. Magn. Magn. Mater. **184**, 89 (1998).

[28] http://materials.springer.com/isp/crystallographic/docs/sd_1823960.

[29] Y. Yang, X. Chen, S. Guo, A. Yan, Q. Huang, M. Wu, D. Chen, Y. Yang, and J. Yang, J. Magn. Magn. Mater. **330**, 106 (2013).

[30] F. Preisach, Z. Phys. **94** (1935).

[31] J. Gräfe, M. Weigand, C. Stahl, N. Träger, M. Kopp, G. Schütz, E. J. Goering, F. Haering, P. Ziemann, and U. Wiedwald, Phys. Rev. B **93**, 014406 (2016).

[32] J. Gräfe, M. Weigand, N. Träger, G. Schütz, E. J. Goering, M. Skripnik, U. Nowak, F. Haering, P. Ziemann, and U. Wiedwald, Phys. Rev. B **93**, 104421 (2016).

[33] R. K. Dumas, C.-P. Li, I. V. Roshchin, I. K. Schuller, and K. Liu, Phys. Rev. B **75**, 134405 (2007).

[34] M. Winklhofer, R. K. Dumas, and K. Liu, J. Appl. Phys. **103** (2008).

[35] J. C. Martinez-Garca, M. Rivas, D. Lago-Cachn, and J. A. Garca, J. Phys. D **47**, 015001 (2014).

[36] M. Rivas, J. Martinez-Garca, and P. Gorria, J. Magn. Magn. Mater. **400**, 315 (2016).

[37] D. Heslop and A. R. Muxworthy, J. Magn. Magn. Mater. **288**, 155 (2005).

[38] C. R. Pike, Phys. Rev. B **68**, 104424 (2003).

[39] J. Gräfe, M. Schmidt, P. Audehm, G. Schütz, and E. Goering, Rev. Sci. Instrum. **85**, 023901 (2014).

[40] H. Kronmüller and M. Fähnle, *Micromagnetism and Microstructure of Ferromagnetic Solids* (Cambridge University Press, Cambridge, 2003).

[41] See Supplemental Material at http://link.aps.org/supplemental/10.1103/PhysRevB.95.024413 for FORC diagrams at 250, 350, and 450 K.